Chiral Terahertz Control via Curvature and Regioselective-Enhanced Reconfigurable Metasurfaces

Jaebeom Lee

nanoleelab@gmail.com

Chungnam National University   https://orcid.org/0000-0002-8414-7290

Juyong Gwak
Chungnam National University

Hyojin Kang
Chungnam National University

Young-Mi Kim
Chungnam National University

Gyuseok Lee
Korea Food Research Institute

Huu-Quang Nguyen
Chungnam National University

Ki-Jae Jeong
CAS Center for Excellence in Nanoscience, National Center for Nanoscience and Technology

Yujin Choi
Chungnam National University

Hee Jun Shin
Pohang Accelerator Laboratory, POSTECH,

Youngjin Cho
Research Group of Food Safety and Distribution, Korea Food Research Institute,

Mahendra Goddati
Chungnam National University

Hongxia Chen
School of Life Sciences, Shanghai University, Shanghai 200444, PR China

Gyeongsik Ok

Article

Keywords: Symmetry breaking, chiral, reconfigurable, metasurface, surface lattice resonances (SLR)

Additional Declarations: (Not answered)

Abstract

Advancements in terahertz (THz) wave photonics necessitate the development of cost-effective and easily manufacturable reconfigurable metasurfaces for dynamically controlling chiral THz frequency shifts. This article introduces two-step innovative approaches to address this need. The first involves integrating a regioselective assembly of magnetoplasmonic nanoparticles (MagPlas NPs) onto a flexible Ni-magnetized metasurface, creating new meta-atoms that induce various resonant frequencies. The second approach integrates curvature with a doped meta-atom to establish easily modifiable chiral systems, thereby enhancing the chiral THz response. The curvature introduces structural asymmetry, disrupting reflection symmetry across the metasurface's symmetry plane, specifically within the split rings. The positions (x, y, z) of the split rings along the curvature can be expressed as symmetry breaking of metasurface=$\Sigma_{i=1}^{n} F(x_i, y_i, z_i, \omega_u)$. When the new meta-atom, regioselective split ring undergoes symmetry breaking due to curvature, the nanoparticles (NPs) act as a lattice, inducing surface lattice resonances (SLR) upon interaction with THz beams and causing strong optical asymmetric interactions. The engineered metasurface using curvature and regioselective assembly has been investigated in terms of enhanced transmittance and reconfigurable chirality by employing various NPs such as Ag@Fe_3O_4 NPs, Void@Fe_3O_4 NPs, and Au@Fe_3O_4 nanorods. By leveraging concepts such as symmetry breaking, magnetized resonators, regioselective magnetic arrangements, and metasurface-enhanced THz response, our study presents a compelling avenue for exerting essential transmittance control and frequency shift over emerging chiral THz reconfigurable systems.

Introduction

A chiral metasurface, characterized by its asymmetry under spatial reflection and composed of periodic exhibits unique electromagnetic properties that distinguish it from naturally occurring materials.[1−6] Controllable nanostructures enable manipulation of THz polarization, facilitating measurement of chiral optical properties, THz imaging, and enhanced material characterization.[7] However, static configurations in conventional chiral metasurfaces limit adaptability, hindering their responsiveness to environmental changes and dynamic radiation shifts.[8−10] Indeed, the induction of a chiral resonance frequency shift in a metasurface conventionally necessitates the manipulation of physical and geometric attributes of the meta-atom.[11,12] To address these challenges, a reconfigurable chiral metasurface was developed that dynamically adjusts its nanostructures in real-time, allowing for on-the-fly control and tuning of electromagnetic properties.[13] This focus is driven by their effectiveness in utilizing selectively chiral polarization, allowing for precise measurement of chiral optical properties, advanced terahertz (THz) imaging, and enhanced optical characterization of materials with specificity and sensitivity.[14,15] However, reconfigurable chiral THz metadevices to dynamically control chirality have a restricted operational frequency range, constraining their utility to specific frequency bands. So, the ability to dynamically control effective chirality represents a transformative advancement with profound implications across various scientific disciplines.[15−17] Nevertheless, integrating these devices with electronic and photonic components is challenging, hindering the correlation of reconfigurable THz optical activity with frequency

shifts.[18,19] Moreover, challenges such as achieving optimal performance within narrow frequency bands, complex fabrication processes, design optimization intricacies, difficulties in seamless integration, and restricted control over specific parameters limit this approach.[20] To overcome this, the integration of metasurfaces with colloidal plasmonic nanoparticles (NPs) stands out as a promising solution, enhancing both signals and device functionality.[21,22] Additionally, it's important to note that coating the metasurface with dielectric materials can also induce a resonance frequency shift.

It is noteworthy that coating the metasurface with dielectric materials can also lead to a shift in the resonance frequency. Surface lattice resonances (SLRs) appear in periodic plasmonic NP arrays due to the hybridization of plasmonic and photonic modes. Compared to localized surface plasmon resonances of single particles, these coupled modes feature reduced linewidth, angle-dependent dispersion, and long-range collectivity. Notably, plasmonic metasurfaces of large periodically arranged nanostructures support collective resonances, *aka.*, SLRs [23−27]. Here the individual responses from the surface plasmons of many individual nanostructures form a collective response that couples to in-plane diffraction orders of the periodic array.[26] Jon *et al.* reported the multispectral metasurface pixel array through the use of colloidal nanocubes larger than 150 nm with a hybrid top-down and bottom-up fabrication to extend the resonance to near-IR.[28] However, indiscriminate coating with dielectric materials not only dampens the inherent properties of the metasurface but also introduces further complexities.

We propose utilizing symmetry breaking and regioselective assembly as a profitable and adaptable method to produce a reconfigurable THz chiral surface capable of controlling frequency shift, intensity, and phase of THz waves. The symmetry breaking occurs, introducing an asymmetry between left and right during the early stages of the specific physical and chemical processes.[29,30] This initial break in symmetry sets the stage for the subsequent emergence of chirality in structures or systems.[31,32] Introducing curvature to the split ring metasurface disrupts its structural symmetry across the entire domain. The regioselective assembly of Magnetoplasmonic nanoparticles (MagPlas NPs), facilitated by an external magnetic field, transforms the initial split ring into a new meta-atom with a lattice configuration. This design is specifically engineered to selectively manipulate THz transmittance and induce optical chiral signals through SLRs and symmetry breaking.

Results

Design and performance of reconfigurable chiral metasurface using curvature. In a typical split ring metasurface (SRM), the resonators are designed to have a mirror-symmetric configuration so that the split rings can show symmetry optical interaction when beam transmits or reflects off the metasurface plane. A THz metasurface of nickel (Ni) split-ring was fabricated on the 120 μm-thick polyimide substrates by utilizing thermal evaporation and lift-off procedure (**Fig. 1a**). The geometrical parameters of each split ring with a thickness of 150 nm were adopted from the best optimized features for responding to THz frequencies elsewhere and further detailed specification is as follows: $A_x = A_y = 58$ μm, inner radius (r_{in}) = 21.2 μm, outer radius (r_{out}) = 25.2 μm, and width = 4 μm. The rings of the unit cells were split

along their diameter into two equal parts with different split angles corresponding to 10° and 40° (**Fig. 1b**). Adding curved geometry to the SRM breaks the structural symmetry of the individual split ring resonators, causing symmetry to be broken at the metasurface level (**Fig. 1b**). The ultimate symmetry breaking was measured at two representative skew angles (*i.e.*, θ = 45°, -45°), which are defined as the angle between the y-axis and tangent vector (**T**) of the metasurface at each maximum LH and RH chirality. A curvature size of 2.25 cm, which had been optimized through prior investigations, was employed.[33] A more detailed correlation between beam chirality and skew angle can be found in previous reports and supporting information (**Fig. S1-1 and S1-2**).[33–36] To obtain the THz optical properties, we utilized THz time-domain spectroscopy (Further experimental details and data can be seen in **Fig. S1-3**. Beam propagates through the center of the metasurface along the z-axis in the experimental condition. The THz beam penetrating metamaterials typically exhibits a size range of approximately 5 to 6 millimeters. This corresponds to a size allowing the beam to pass through approximately 10x10 split rings. In our measurements, we employed a linearly polarized laser beam from regenerative amplifier system. A circularly polarized beam (CPB) can be generated by utilizing a quarter-wave plate. When the linearly polarized beam passes through the quarter-wave plate, it transforms into a CPB. We utilized a commercially available quarter-wave plate for this purpose. By adjusting the angle of the wave plate to 45°, an right circularly polarized (RCP) beam is achieved and rotating it to -45° results in an LCP beam (**Fig. 1c**). The quality of the CPB is contingent upon the angle of the quarter-wave plate. To achieve optimal CPB, we employed a Wollaston polarizer to separate the two components of S and P polarization in the CPB. Subsequently, we fine-tuned the angle of the quarter-wave plate to ensure equality between the S and P polarized components of the beam. The extrinsic chirality mechanism of symmetric structures excited by non-vertically incident electromagnetic waves like LCP or RCP, can be investigated by examining the wave vector properties in momentum space. In instances where the metasurface remains flat and interacts with either LCP or RCP waves, the observed transmittance predominantly indicates no difference (**Fig. 1d**). This is because the electromagnetic wave vector is no longer perpendicular to the metasurface, but the flat metasurface does not show the asymmetric signal between LCP and RCP. Therefore, it is inaccurate to classify such materials as chiral substances.

Meanwhile, when a metasurface exhibits curvature and interacts with either LCP or RCP waves, the alterations in the observed transmittance can be attributed to the distinctive properties of the electromagnetic wave vector. In the context of curved metasurfaces, the electromagnetic wave vector is no longer perpendicular to the surface, giving rise to what is known as curved chirality. This curvature-induced change in the orientation of the wave vector results in different extrinsic chirality effects compared to those observed with a flat metasurface depending on the LH (**Fig. 1e**) and RH (**Fig. 1f**) structure. Therefore, the variations in transmittance observed under these conditions can be explained by the impact of the curved metasurface on the direction and characteristics of the electromagnetic wave vector. In detail, **Fig. 1e** presents that the transmittance derived from the interaction of the LCP with the left-handed (LH) structure of a metasurface with a skew angle of 45˚ was higher than the RCP up to 1425 GHz frequency, but at the above 1425 GHz, the LCP showed a lower transmittance than the RCP. However, the RH structure on the metasurface with a skew angle of -45˚ showed the opposite transmittance

compared to the LH at 1350 GHz, depending on the orientation of the CPB (**Fig. 1f**). These asymmetric optical interactions induce differential responses to LCP and RCP beam depending on the skew angle, allowing the metasurface to exhibit chiroptical properties in the interaction with CPB. This indicates a clear determination of LH structure at a skew angle of 45° and RH structure at -45°. The chiropractic properties of SRMs (**Fig. S1-4**) with curvature were also studied by computational simulations (finite difference time domain (FDTD) method) with curved split ring layer geometry (**Fig. S1-5 and S1-6**). Moreover, when considering transmittance values alone, it is crucial to note that the chiral metasurface with curvature (RH: 0.61) lags the flat metasurface, which displays an average of 0.77, indicating a decrease of approximately 0.16. This is because curvature can change the beam path, potentially increasing losses through higher reflection and scattering on the curved metasurface, resulting in reduced transmittance. To overcome the limitations in transmittance intensity observed when applying curvature, the approach of regioselective assembly will be elaborated in detail in Figs. 3 and 4.

Circular dichroism (CD) is a spectroscopic technique with broad applicability, extending beyond individual molecules to encompass diverse materials, including chiral metasurfaces. In the context of inquiry involving a chiral metasurface and THz beams, CD can be instrumental in characterizing the metasurface's chirality. When a chiral metasurface interacts with THz beams, the CD spectrum manifests as variations in the transmitted intensity between LCP and RCP components. This distinctive pattern serves as a signature fingerprint, revealing information about the metasurface's chiral properties. In SRMs with skew angles of 0° or 180°, the resonators are designed to have mirror symmetry, such that the shape and orientation of the split rings are identical when reflected in the symmetry plane (**Fig. 1f**). This mirror symmetry ensures that the metasurface behaves similarly in both LCP and RCP beam, which means this structure is achiral. However, if a skew angle of 45° or -45° is introduced into the split ring resonator, the mirror symmetry is strongly broken, which highbeams that it is chiral. This is evident in **Fig. 1f**, where the signals of RH and LH structures are symmetrical. That means the transmittance when interacting with LCP is higher than when interacting with RCP in the LH structure. Conversely, in the RH structure, the transmittance when interacting with RCP beam is higher than when interacting with LCP beam. These outcomes signify that a curvature-based metasurface exhibits optically asymmetric signals. In detail, the equation $\omega_u = Lu$, where $u = (H, E, P, J)$ Ⓧ establishes a condition of symmetry in the context of the split-ring metasurface.[37−39] Here, ω_u signifies the result of the matrix operation L acting on the vector **u**. The vector **u** encompasses four critical components: H (magnetic field), E (electric field), P (polarization), and J (current density). This equation indicates that, under specific circumstances, the transformation induced by matrix L preserves the symmetrical characteristics of the metasurface. In essence, it implies that there are defined relationships between the magnetic field, electric field, polarization, and current density within the metasurface structure, allowing for consistent and symmetrical behavior in response to external factors or interactions. The curvature introduces a structural asymmetry that cannot be preserved in reflection across the symmetry plane. The symmetry breaking of the metasurface can be articulated as follows;[39]

$$Symmetry\,breaking\,of\,metasurface = \sum_{i=1}^{n} F\,(x_i,\,y_i,\,z_i,\,\omega_u)$$

The function F represents the influence of curvature on the split ring, denoted as **F (x, y, z, ω_u)**. This function encapsulates the alterations that occur in the split ring's behavior as a result of the introduced curvature. It accounts for how the position of the split ring in terms of its coordinates (x, y, z) and the transformed vector ω_u, which represents the state of the system, are affected. Essentially, F quantifies the impact of curvature on the overall symmetry and response of the metasurface. In the presence of curvature, the split ring's position (x, y, z) can be altered. This implies that configurations like (x, y, z), (-x, y, z), (x, -y, z), and so on, may come into play. Despite these potential variations, when the skew angle is set at 0, 90, 180, 270, or 360 degrees, symmetry is maintained.[33,34] However, at other skew angles, symmetry is disrupted. Notably, at angles such as 45 and − 45 degrees, which are the furthest removed from the aforementioned symmetric angles, the most significant symmetry breaking occurs. This observation underscores the sensitivity of symmetry maintenance to skew angles and highbeams the pronounced effect at certain non-standard angles like 45 and − 45˚. Curvature induces chirality by disrupting the mirror symmetry of split rings in the metasurface, creating an asymmetrical spatial arrangement that leads to distinctive chiroptical properties in response to CPB. The chirality arising from symmetry breaking due to curvature represents a unique mechanism, diverging from conventional metasurfaces that induce chirality by altering their own structure or alignment; this metasurface-level asymmetry deviates from traditional chiral behavior.

Tuning Resonances in SRM through Magnetic Field Modulation. In the initial design of split-ring type metasurfaces, dominant resonances can be observed in which high-frequency dipole-type electrical resonances are attributed to interactions between SRM sides or components parallel to the incident electric field.[40] The interaction between the magnetic field (H), resonant electric field (E), and induced current (J) can alter the overall magnetization behavior of the SRM. Thus, the orientation of the external magnetic field can indirectly affect the electrical resonance by modifying the overall response of the metasurface. Ni SRMs can therefore exhibit different magnetization depending on the orientation of the external magnetic field (Fig. 2a). To optimize the magnetization time of the Ni SRMs, they were magnetized in either the x- or y-axis direction at 87–90 mT for 0.1 h. The magnetization was visible in the magnetic force microscopy (MFM) images (**Fig S2-1**). The magnetized Ni split-ring is a typical ferromagnetic material, and its magnetic properties can be differently stimulated depending on the direction of magnetization. So, the magnetization of Ni split-ring was simulated depending on the x- (Fig. 2b**)**, y-axis magnetic field direction (Fig. 2d) and in the absence of magnetic field (**Fig S2-2**). The simulation results showed that the narrow gap of the Ni split ring induces a significantly stronger magnetic field along the x-axis magnetization (Fig. 2c**)** than the y-axis magnetization (Fig. 2e**)**, which influences the further self-assembly of MagPlas NPs. In addition, depending on the direction of the magnetic field, MagPlas NP resonances can be incorporated into SRMs in the THz region to enhance frequency-induced capacitive resonance. The incorporation of skew angle and selective alignment of MagPlas NPs using external magnetism introduces a new dimension of control over metasurface behavior, distinguishing it from previous research endeavors.

Regioselective assembly of MagPlas NPs on flat Ni-Metasurface for tailored responses. This novel approach empowers precise manipulation of plasmonic NPs on the flat Ni-metasurface, enabling tailored responses to linear polarized incident THz optical rays. By strategically assembling NPs and nanorods (NRs), each with distinct characteristics, we gain insights into their nuanced interactions within the THz region. Moreover, the optimization of deposition parameters, such as time, concentration, and surface density, fine-tunes the metasurface's performance, offering a systematic methodology for achieving desired outcomes. To characterize the interaction of plasmonic NPs to incident THz optical rays, three different MagPlas NPs or NRs were prepared to be regioselectively assembled in the Ni-metasurface as an enhancing tool in the THz region: $Ag@Fe_3O_4$ core-shell NPs (Fig. 3a) with an average diameter of 175 nm, its hollow (void@Fe_3O_4) NPs for comparing plasmonic effect (Fig. 3b); and in particular, 1-dimensional $Au@Fe_3O_4$ NRs that have the average diameter and length of the NR was 226 nm and 1.035 µm while the diameter of Au core was 51 nm (Fig. 3c). The details of the synthesis and treatment can be found in the **Fig S3-1**.[41] The magnetic properties of MagPlas NPs/NRs were measured by using superconducting quantum interference device (SQUID), reaching to ~ 60 emu/g, which shows soft ferromagnetic properties (**Fig S3-2**). **Fig S3-3 and S3-4** present the unique optical properties and size distribution profiles of NPs and NRs. The SEM and THz time domain spectroscopic analysis of the regioselective metasurface were carried out depending on the magnetization direction (X and Y axis). The magnetization time was optimized to 0.1 h while The MagPlas NPs/NRs were deposited selectively on the magnetized Ni split-ring for 0.1 ~ 12 h (**Fig S3-5**). The deposition concentration of NRs was also optimized in the range of 0.1 ~ 1 mg mL^{-1}, then the surface density of the deposited particles was optimized to be 0.3 mg mL^{-1}. (See further details of the optimization process in **Fig S3-6**.) Then, MagPlas NP (1 mg mL^{-1}), hollow NPs (1 mg mL^{-1}), or NR (0.3 mg mL^{-1}) solution was deposited on the magnetized Ni patterns for 0.1h, respectively, where the surface density of the deposited NPs and NRs is nearly identical, as visible in the SEM images (Fig. 3d-i). The strong narrow gap (the dashed box) in Ni split-ring along the x-axis magnetization was completely linked with assembled NPs (Fig. 3d-f) while, in the y-axis magnetization, NPs and NRs are assembled on the pattern, preserving the original gap for THz signaling (Fig. 3g-i). Different bathochromic shifts were observed with the deposition of various concentrations of MagPlas NPs/NRs under the X-axis magnetization. Both 0.1 mg of MagPlas and hollow NP present 26 GHz and NRs present 46 GHz (**Fig S3-7**). This sbeam shift probably results from incomplete NP deposition on the designated area of the Ni-metasurfaces as shown in **Fig S3-8**. Meanwhile, as the deposition concentration was increased up to 1 mg for NPs and 0.3 mg for NRs, respectively, the peak shift of THz spectra under the X-axis magnetization was remarkable at all samples, shifting to 1280 → 1175 (Δ105), 1265 → 1213 (Δ52), and 1278 →1148 (Δ130) GHz (Fig. 3j-m).

The lattice structure possesses unique refractive properties, allowing for controlled manipulation of transmitted beam at specific angles. In comparison to the non-regioselective assembly, metasurfaces assembled with regioselective NPs exhibited an approximately 15% reduction in transmittance intensity. This reduction is attributed to the lattice's capacity to impart specific refractive characteristics to transmitted beam, leading to redirection at particular angles. The regioselective assembly of NPs on the metasurface introduces a spatial arrangement that, upon interaction with a linearly polarized THz beam,

results in modified transmittance characteristics. This observed behavior is consistent with the refractive properties induced by the lattice structure, influencing transmitted beam in alignment with the specific refractive attributes of the lattice. The results can be correlated with the particle size and polarization as well as assembled position and structure in the pattern, ultimately allowing for tailored resonant near-fields in the split-ring pattern. Moreover, when paired with plasmonic materials like metallic NPs or thin films, split-ring nanostructures are influenced not only by SLRs but also by the dielectric material coating on the NPs themselves. This dual influence impacts both transmittance intensity and frequency shifting within the THz ranges. [42,43] The high aspect ratio of the rods, which may not perfectly conform to the regioselective assembly of split rings, is noteworthy. It is crucial to recognize that, in terms of the refractive index of the dielectric material coating, the impact on transmittance changes may be relatively pronounced compared to isotropic NPs. Overall, the novel meta-atom concept formed by regioselective assembly on a flat metasurface suggests that the regioselective assembly as lattice structure of may not exhibit optimal transmittance effects in interaction with linear polarized beam.

This applies along the X-axis as well, and all samples exhibit a higher peak shift along the X-axis compared to the Y-axis. It is important to note that unnecessary linkages among the split ring unit may induce the unspecified resonant frequencies of the inherited THz wave. Indeed, the highest peak shift in the Y axis appeared at the NRs deposition in 1278 → 1141 GHz, reaching 137 GHz of the frequency shift, which is currently the largest frequency shift reported so far (Fig. 3m). Therefore, it is probable that particle shape and concentrations, and magnetization direction are major parameters to enhance frequency shift. Further simulation study was carried out to explain the current observation in depth **(Fig. S3-9 and S3-10)**. In addition, the hollow NPs doped at Ni patterns show the different THz wave in magnetized metasurface at both X- and Y- directions (Fig. 3j **and k**).

Enhancing optical asymmetry in reconfigurable Chiral THz metasurfaces: A comprehensive analysis of regioselectively assembled MagPlas NPs. The regioselective THz metasurface of nickel (Ni) split-ring could be successfully fabricated to the reconfigurable chiral metasurface by introducing the skew angle (45°, -45°) depending on the (Fig. 4a) MagPlas NPs, hollow magnetic NPs (Fig. 4b) and Au@Fe$_3$O$_4$ NRs (Fig. 4c). It could be providing a visual representation of the time-dependent circularly polarized THz transmittance across all regioselective LH and RH metasurfaces (Fig. S4-1). To conduct a more detailed analysis of these changes in relation to frequency, we applied the FFT to the magnitude-frequency data (Fig. S4-2). Overall, the interaction between regioselective assembly and PCL was observed to result in transmittance peaks at frequencies of 1200 and 1500, regardless of the curvature direction (LH and RH). When MagPlas NPs are arranged in a lattice-like structure within a LH metasurface with a 45° skew angle, a higher transmission interaction is observed with LCP than RCP starting from a frequency of 1200 GHz. This arrangement exhibits enhanced transmittance when compared to the non-regioselective counterpart (0.71→0.88) (Fig. 4d). Conversely, when MagPlas NPs are arranged in a lattice-like structure within a RH metasurface with a -45° skew angle, a lower transmission interaction is observed with LCP than RCP from a frequency of 1200 GHz. Despite this, the arrangement still exhibits enhanced transmittance compared to the non-regioselective counterpart (0.62→0.73) (Fig. 4g). Additionally, an intriguing observation was

the relatively lower transmittance exhibited in the RH compared to the LH configuration in the 1500 frequency range.

Expanding on the Fig. 3 discourse, delving into the intricacies of regioselective assembly within metasurfaces exhibiting curvature becomes pivotal. In deviation from the typical trend observed in non-regioselective LH metasurfaces with curvature, regioselective assemblies with curvature manifest a pronounced increase in transmittance after interaction with an LCP beam (Fig. 4b). This phenomenon underscores a distinctive interplay between curvature and circular polarization. The augmented transmittance observed in regioselectively assembled metasurfaces with curvature can be attributed to heightened chiral effects facilitated by the specific spatial arrangement of NPs. In this context, the nanostructures, acting as a lattice, assume an orderly chiral configuration in response to the curvature. This organized chiral arrangement, when subjected to interaction with CPB, has the potential to selectively induce asymmetric interactions within specific frequency domains (ex, 1200, 1500 frequency). In essence, the regioselective assembly of NPs in the metasurface, acting as a lattice structure, can lead to a chiral organization influenced by the curvature. This, in turn, gives rise to enhanced chiral effects that selectively induce asymmetric interactions, particularly in certain frequency ranges, when interacting with CPB.

In contrast, the incorporation of hollow@Fe_3O_4 onto the metasurface leads to a limited transmittance efficiency from 0.71 to 0.75 at the LH structure (Fig. 4e), but increased from 0.62 to 0.71 at the RH (Fig. 4h). This limited enhancement in transmittance, accentuating the restricted influence of Surface Lattice Resonance (SLR), is attributed to the structural characteristics and the incomplete exploitation of SLR in hollow@Fe_3O_4 compared to Ag@Fe_3O_4 under a circularly polarized THz beam.[44] Despite this, the similar asymmetric signal behavior to Ag@Fe_3O_4 in the 1200 and 1500 frequency, can be elucidated by the fact that the hollow nanostructure does not disrupt optical asymmetry interaction.

The elongated morphology of the Au@Fe_3O_4 NRs may lead to reduced field confinement and localization, presenting a contrast with the more compact NPs. This structural distinction may not be optimally conducive to SLR. In the left-handed (LH) structure, the rod transmittance (0.79) exhibited a relatively higher value compared to the hollow transmittance (0.75) (**Fig. 4e, f**). Conversely, in the right-handed (RH) structure, a decrease in transmittance (0.66) was observed for hollow compared to the hollow transmittance (0.71) (**Fig. 4h, i**). This irregularity can be attributed to the alignment disruption arising from the structural features of the nanorods. Nevertheless, despite these variations, the asymmetrical behavior aligns with the trend observed in MagPlas NPs, indicating a similar tendency in terms of wavelength-dependent transmittance characteristics. As a result, the integration of NRs significantly disrupts the overall efficiency of the metasurface in its interaction with THz waves.

The observed frequencies, namely around 1200 and 1500 GHz, are likely indicative of the selective resonant properties associated with the specific SLR and lattice effect utilized in the investigation, including Ag@Fe_3O_4 NPs, Hollow NPs, and Au@Fe_3O_4 NRs. This enhancement manifests in improved transmission properties, increased polarization selectivity, and the potential for various applications,

including chiral sensing, polarization manipulation, and efficient manipulation of frequency shift. Hence, we aimed to systematically assess the optical activity capabilities of the engineered metasurface, particularly in terms of its effectiveness in polarization manipulation and efficient control of THz waves.

The described experiment aimed to validate the regioselective assemble metasurface's ability to induce CPB, also known as optical activity. This optical activity is contingent on the specific configuration of the regioselective metasurface. The verification process involved directing linearly polarized beam onto the metasurface at a 0° angle, as outlined in **Scheme 1**. Subsequently, the beam passed through the metasurface and a wire grid polarizer. The polarizer's orientation was meticulously rotated at angles of θ_{rot} = -6°, -4°, -2°, 0°, 2°, 4°, and 6°, allowing for a detailed examination of variations in transmittance intensity centered around an angle of incidence of 0 degrees. To elaborate further, it is crucial to note that the observed patterns in specific frequency transmittance intensity (ex, 1120, 1420, 1570 GHz) were key indicators of the metasurface's controllable chiral structure. For instance, if the change of transmittance intensity shows a disordered rather than a linear one depending on the angle of the polarizer, it indicates an inability to control the chiral structure. On the contrary, a consistent change of transmittance intensity depending on the xx suggested a controllable chiral structure. This predictability implied that beam consistently rotated in either the LH or RH direction depending on the curvature's - or + direction. To ensure the reliability and robustness of the findings, each experiment was meticulously repeated four times.

Validating controllable chirality: Experimental analysis of CPB induction in Regioselective Metasurfaces.
The time-varying THz transmittance across the regioselective LH and RH metasurface of $Ag@Fe_3O_4$ NPs (**Fig S5-1**), Hollow NPs (**S5-2**), and $Au@Fe_3O_4$ NRs (**S5-3**) dependent on the θrot was measured.To closely analyze changes in transmittance to frequency, we conducted FFT using magnitude-frequency data (See **Fig S5-4, S5-5, S5-6**). The analysis in **Fig. 4** provided a comprehensive examination of the metasurface's behavior at different frequencies. The results conclusively demonstrate that our metasurface displays a notable propensity to induce frequency shift and asymmetric transmission within the frequency bands of 1100 and 1500 GHz, particularly in the context of chiral-selective interactions depending on the regioselective materials. The distinctive behavior observed can be attributed to the selectively induced electromagnetic wave vector from the structural composition of SLR and symmetry breaking, making it exceptionally receptive to incident radiation within these specific frequency ranges. When CPB THz interacts with this system, it selectively enhances chiral transmittance, exhibiting an increase in transmission for the composition of chiral SLR. The intentional choice of frequencies, specifically 1120, 1420, and 1570 GHz, is associated with the enhanced chiral transparency observed at approximately 1200 and 1500 GHz by the integration of SLRs. This deliberate choice anticipates a harmonization between these frequencies and the inherent plasmonic resonances of the chosen materials, thereby augmenting the selective chiral transmittance.

Consequently, utilizing **Fig S5-4, S5-5, and S5-6**, we conducted a comprehensive analysis of how ellipticity evolves based on the regioselective metasurface in the (i) 1120, (ii) 1420, and (iii) 1570 GHz frequency ranges. Initially, an in-depth analysis was performed using the $Ag@Fe_3O_4$ regioselective metasurface.

asymmetric signals were confirmed, contingent on LH and RH structures in each section (Fig. 5a). The material in question exhibits both structural and optical isotropic properties. When MagPlas NPs align with the x-axis of the magnetic field on the Ni split ring, they tend to exhibit consistent behaviors, including J. This implies that when particles are aligned in a regioselective manner, they can orient themselves within the metasurface without significant deviation from the $\sum_{i=1}^{n} F$ (x_i, y_i, z_i, ω_u) equation, even in the presence of curvature-induced symmetry breaking. This leads to asymmetric interaction with THz beam, resulting in asymmetric E and P between LH and RH structures. As a result, distinctive chirality becomes noticeable at alignments of 45° and – 45°. To elaborate, the change in transmittance for the regioselective LH structure is indicated by a red line, while for the RH structure, it is represented by a blue line, depending on the θ_{rot} angle. Specifically, the transmittance follows an elliptical trajectory, increasing from 4˚ to -2˚, and then gradually decreasing to -4˚ at 1120 GHz (Fig. 5a-i). This phenomenon underscores that when linearly polarized beam traverses the metasurface, it undergoes a conversion into left circularly polarized beam (LCPB) in a specific direction. Conversely, the discernible trend of the blue line (representing RH) shows an increase along an elliptical path from – 4˚ to 2˚, followed by a decline at 4˚. This signifies that linearly polarized beam passing through the LH metasurface undergoes a rotation into RCP in a specific direction. Similarly, in the 1420 (Fig. 5a-ii) and 1570 (Fig. 5a-iii) GHz ranges, the asymmetry between LH and RH structures exhibits a trend like that observed at 1120 GHz. However, transmittance intensity is highest at 1120 GHz. This indicates that Ag@Fe$_3$O$_4$ demonstrates optimal chiral conversion in the 1120 GHz range.

Examining the Hollow structure using a similar methodology yields intriguing findings (Fig. 5b). Hollow particles, owing to their structurally isotropic nature, can achieve alignment within specific bounds without significant deviation from $\sum_{i=1}^{n} F$ (x_i, y_i, z_i, ω_u). However, due to their hollow interior, factors such as refractive index can undergo substantial variations when THz waves permeate the particles. Specifically, at 1120 GHz, the LH structure exhibits a progressive decrease in transmittance from – 6° to 6°, while the RH structure does not display the same trend (Fig. 5b-i). This can be attributed to a lower chiral conversion ability at 1120 GHz, potentially resulting from the various refractive index changes induced by the core structure. Additionally, compared to Ag@Fe$_3$O$_4$, the transmittance intensity is relatively lower. This distinction arises from the incorporation of hollow magnetic NPs (void@Fe$_3$O$_4$), which does not generate distinct resonant modes or alter the SLRs of the metasurface. In contrast, at 1420 (Fig. 5b-ii) and 1570 GHz (Fig. 5b-iii), a relatively high chiral conversion ability is observed. Moreover, the intensity variations at different angles are minimal, implying lesser impact on ellipticity. From these observations, it can be inferred that the regioselective metasurface with a Hollow structure demonstrates optimal chiral conversion at 1420 GHz.

Next, we conducted an in-depth analysis of the regioselective metasurface with a rod structure (Fig. 5c). Unlike NPs, the rod structure is not optically isotropic. Irregular coating of the metasurface with dielectric materials can also lead to obvious frequency shift due to the unconsistant lattice but chiral resonance frequency movement cannot show consistency. In detail, aligning rods within the metasurface may present challenges in conforming to the equation $\sum_{i=1}^{n} F$ (x_i, y_i, z_i, ω_u) in comparison to other particles.

When MagPlas NRs align with the x-axis of the magnetic field on the Ni split ring, they could exhibit irregularities and accommodative behaviors, including J, compared to NPs. This discrepancy in alignment becomes particularly relevant when introducing external LH and RH curvatures. Such deviations from ideal alignment can hinder the clear chiral interaction with THz radiation, resulting in weak asymmetric E and P. These weakened fields diminish the metasurface's ability to induce a robust chiral response when subjected to THz beam, underscoring the importance of precise alignment for optimal performance in chiral metasurface applications. For instance, the LH structure exhibits a consistent decrease from − 6° to 6° at 1120 GHz (Fig. 5c-i). In contrast, the RH structure displays a sharp decrease from − 6° to 4°, followed by a steep increase from − 4° to -2°, then a gradual rise from − 2° to 2°, and finally a decline from 2° to 4°. This observed trend is attributed to the high aspect ratio of the rods, which may not perfectly conform to $\sum_{i=1}^{n} F$ (x$_i$, y$_i$, z$_i$, ωu) within the regioselective assembly of split rings (Fig. 5c-i). However, at 1420 GHz, both RH and LH demonstrate a similar increase and decrease trend, ranging from − 6 to 0, before displaying opposite signals from 0° to 4° (Fig. 5c-**ii**). Conversely, at 1570 GHz (Fig. 5c-**iii**), relatively stable chiral conversion abilities are observed. However, the intensity variations with respect to angles are minimal, indicating lower ellipticity. In the case of rods, it's worth noting that the results for LH and RH structures may exhibit some asymmetry, potentially resulting in lower chiral conversion abilities. It unveiled unclear asymmetries, providing unequivocal evidence of the regioselective chiral metasurface inherent optical activity (Fig. 5c-**iii**). All results demonstrates that the linear THz signal exhibits unique optical activity when interacting with a regioselective metasurface with a skew angle depending on the configuration of the SLR. Indeed, the observed phenomenon strongly implies that, regardless of the incident angle, all metasurfaces exhibit higher THz transmittance in LH configurations compared to RH configurations (Fig. 5d). This intriguing behavior might be arising from a combination of the presence of the nickel split ring and the rugged nature of the NPs. Even when the NPs align due to an applied external magnetic field, the complex interplay between these factors is sufficient to induce a pronounced left-handed alignment. Consequently, this structural configuration can be effectively designed as cascaded chiral metamaterials, displaying enhanced selectivity particularly in LH configurations.[45] This deduction underscores the significance of structural considerations in achieving desired THz response characteristics.

Discussion

In conclusion, this study explored a novel approach in creating a regioselective chiral metasurface utilizing Ni split-ring resonators. By introducing a skew angle, the symmetrical condition of the split ring resonators, ω$_u$ = Lu was intentionally disrupted. This led to change split ring's F (xi, yi, zi, ωu) and asymmetric optical interactions with circularly polarized THz beam. Specially, the selective alignment of isotropic NPs depending on the magnetization direction demonstrated consistent orientation in the split ring's F (xi, yi, zi, ω$_u$), leading to noteworthy selective enhanced transmttance in the THz spectra compared with anisotropic MagPlas rods. Moreover, the integration of MagPlas NPs, Hollow NPs, and MagPlas rods onto the chiral metasurface with curvature substantially enhanced the transmittance of the capacitive resonance compared to the non-regioselective assembly after interacting with the LCP and

RCP beam. It could be induced by the integrations of SLR further improve the transmission efficiency and chiral polarization selectivity of the metasurface compared with Hollow NPs. Moreover, this validated the ability of the metasurface to induce optical activity, specifically circular polarization, when exposed to linearly polarized beam. Consequently, MagPlas NPs exhibit the most effective chiral conversion at the frequency of 1120 GHz and Hollow NPs at 1420 GHz. Meanwhile, irregular coating of the NRs regioselective assembly on the metasurface could lead to an unconsistent lattice and optical chirality movement also cannot show consistency. The incorporation of skew angle and selective alignment of NPs using external magnetism introduces a new dimension of control over metasurface behavior, distinguishing it from previous research endeavors. These findings hold substantial implications for applications in a myriad of fields including optics, telecommunications, and nanotechnology like in chiral sensing, polarization manipulation, and efficient manipulation of THz waves.

Materials and methods

General Procedures

Ferric nitrate nonahydrate ($Fe(NO_3)_3 \cdot 9H_2O$), ferric chloride hexahydrate ($FeCl_3 \cdot 6H_2O$), sodium citric ($C_6H_5Na_3O_7 \cdot 2H_2O$), sodium acetate ($CH_3COONa$, NaAc), sodium borohydride ($NaBH_4$), silver nitrate ($AgNO_3$), ethylene glycol (EG, $HOCH_2CH_2OH$), diethylene glycol (DEG, $(HOCH_2CH_2)_2O$), oxalic acid (OA, $H_2C_2O_4$), 4-nitrophenol (4NPol), 1-ethyl-3-(3-dimethylaminopropyl)carbodiimide (EDC, $C_8H_{17}N_3$) and N-hydroxysuccinimide (NHS, $(CH_2CO)_2NOH$) were used. Deionized (DI) water (18 MΩ cm^{-1}) was used for all solution preparations and experiments.

Synthesis

Ag@Fe$_3$O$_4$ NPs

Fe $(NO_3)_3 \cdot 9H_2O$ (0.1 M) was completely dissolved in 40 mL of EG, followed by the addition of NaAc (0.875 M) and $AgNO_3$ (14.75 mM). The mixture was vigorously stirred for 60 min and then sealed in a Teflon-lined stainless-steel autoclave (volume, 50 mL). The autoclave was heated at 200°C for 8 h and then allowed to cool to 25°C. The black products were washed with ethanol and DI water three to five times and then dried under vacuum conditions at 60°C for 6 h.

Hollow@Fe$_3$O$_4$ NPs

An 18 mg of bare Ag@Fe$_3$O$_4$ NPs, not stabilization one, is added into 60 mL distilled water followed by the addition of 1.17 g NaCl. The mixture is sonicated for 10 minutes. After that, the solution is ultrasonicated by ultrasonic probe (5 sec on, 15 sec off) for more than 72 h. After that, the product is washed several times with distilled water and ethanol and then dried under vacuum at 60°C for 6 h.

Au@Fe$_3$O$_4$ NRs

Au@Fe$_3$O$_4$ NRs were synthesized using a previously described one-pot solvothermal method.[46] In brief, FeCl$_3$·6H$_2$O (0.1 M) was dissolved in a mixture of EG and (40 mL, 1:1 volume ratio) to form a clear yellow solution, followed by the addition of sodium acetate (0.875 M) and HAuCl$_4$·3H$_2$O (14.75 mM). The mixture was stirred vigorously until all the reactants were fully dissolved. The obtained suspension was then transferred to a 50 mL. Teflon-lined stainless-steel autoclave and heated at 200°C for 8 h. The black products were washed with ethanol and DI water three to five times and then dried under vacuum conditions at 60°C for 6 h.

Analysis and instrument

DLS, TEM, SEM, AFM and MFM

The surface potentials and particle size distributions of Ag@Fe$_3$O$_4$ NPs and hollow NPs were monitored using a Zetasizer (ZS Nano, Malvern Instruments, Malvern, U.K.). The morphologies, sizes, and magnetic properties of the Ag@Fe$_3$O$_4$ NPs and hollow NPs were characterized by high-resolution transmission electron microscopy (HR-TEM) (JEM-3010, JEOL, Tokyo, Japan), field-emission scanning electron microscopy (FE-SEM) (S-4700, Hitachi, Japan), optical microscopy (DM2000, Leica, Wetzlar, Germany), Atomic force microscopy (AFM), and magnetic force microscopy (MFM) (Innova, Veeco, Plainview, NY). The magnetic properties of Ag@Fe$_3$O$_4$ NPs are checked using a superconducting quantum interference device-vibrating sample magnetometer (SQUID-VSM) (MPMS 3, Quantum Design, San Diego, CA).

THz-TDS

Fig S1-3 shows scheme of transmission-mode THz-time domain spectroscopy (TDS) system (TPS-3000, Teraview, Cambridge, UK). The femtosecond pulses were produced by a Ti:Sapphire laser with a central wavelength of 800 nm and a pulse width of 90 fs. The ultrashort pulse is divided into a pump and probe beam using a beam splitter. One of the beams was focused on a photoconductive antenna (PCA) fabricated with a Ti/Au dipole antenna to emit THz waves, and the other beam is used to detected THz pulse.[47] The generated THz pulse is focused with gold coated ellipsoidal mirror, and the THz beam size of the focused THz pulse is about 4 mm at the sample position. And the transmitted THz pulse through the sample is detected by another photoconductive antenna gated by the probe beam. The environment of experiments was enclosed in a chamber and purged with N$_2$ to eliminate the THz absorption by water vapor in air at 25°C.

The THz-TDS system utilized a 1 kHz regenerative amplifier laser with a central frequency of 800 nm and a pulse duration of 120 fs in fs-THz beamline located at Pohang Accelerator Laboratory (PAL). The output of the regenerative amplifier laser was split into two distinct paths, one dedicated to THz pulse generation and the other for detection. In the former path, the laser beam passed through a 20 mm × 20 mm × 2 mm ⟨110⟩ ZnTe crystal to produce THz pulses via optical rectification. Meanwhile, the latter beam was employed for THz field detection through electro-optic sampling, making use of a 5 mm × 5 mm × 1 mm ⟨110⟩ ZnTe crystal.

Circularly polarized THz beam

In our measurements, we employed a linearly polarized laser beam from regenerative amplifier system. A circularly polarized beam can be generated by utilizing a quarter-wave plate. When the linearly polarized beam passes through the quarter-wave plate, it undergoes a transformation into a circularly polarized beam. We utilized a commercially available quarter-wave plate for this purpose. By adjusting the angle of the wave plate to 45°, a RCP beam is achieved and rotating it to -45° results in a LCP beam. The quality of the circularly polarized beam is contingent upon the angle of the quarter-wave plate. To achieve optimal circular polarization, we employed a Wollaston polarizer to separate the two components of S and P polarization in the circularly polarized beam. Subsequently, we fine-tuned the angle of the quarter-wave plate to ensure equality between the S and P polarized components of the beam.

FEM simulations

The local field enhancement effect and THz-time domain spectroscopy spectra were computationally calculated using FEM simulation (COMSOL Multiphysics version 5.2a, COMSOL AB, Stockholm, Sweden). The frequency domain calculations were performed in the Wave Optics module, in which the dimensions of the Ni-imprinted metasurface with open ring geometries were similar to the experimental conditions. The NPs were treated as scaled microsized particle clusters to reduce meshing complexity, in which the scaling factor were selected at 10 when $Ag@Fe_3O_4$ NPs were coated on the metasurface, and 2 when $Au@Fe_3O_4$ NRs were coated on the metasurface. THz-time domain spectra were calculated in interval of 10 GHz outside of the peak absorption area (1400 to 1600 GHz), and 1 GHz at the peak absorption area.

Declarations

Acknowledgments

Conflict of interest

The authors declare no competing interests.

Author contributions

J.G., J.L., G.O., Y.K., and K.J. designed and supervised the project. J.G., H.K., Y.K. and Yu.C. performed the experiments. H.N. provided the materials. G.L., Y.C. and G.O. performed the simulation. J.G., H.S. and J.L. performed the data analysis. J.G., J.L. G.O., Y.K., and G.L. wrote the manuscript. All co-authors edited the manuscript.

References

1. Seo, M. A. *et al.* Terahertz field enhancement by a metallic nano slit operating beyond the skin-depth limit. *Nature Photonics* **3**, 152-156, doi:10.1038/nphoton.2009.22 (2009).

2. Yu, N. *et al.* Light propagation with phase discontinuities: generalized laws of reflection and refraction. *science* **334**, 333-337 (2011).

3. Gansel, J. K. *et al.* Gold helix photonic metamaterial as broadband circular polarizer. *science* **325**, 1513-1515 (2009).

4. Zhao, Y., Belkin, M. & Alù, A. Twisted optical metamaterials for planarized ultrathin broadband circular polarizers. *Nature communications* **3**, 1-7 (2012).

5. Yin, X., Schäferling, M., Metzger, B. & Giessen, H. Interpreting chiral nanophotonic spectra: the plasmonic Born–Kuhn model. *Nano letters* **13**, 6238-6243 (2013).

6. Kang, L. *et al.* An active metamaterial platform for chiral responsive optoelectronics. *Advanced Materials* **27**, 4377-4383 (2015).

7. Wang, P. *et al.* Terahertz chiral metamaterials enabled by textile manufacturing. *Advanced Materials* **34**, 2110590 (2022).

8. Liu, M., Powell, D. A., Shadrivov, I. V., Lapine, M. & Kivshar, Y. S. Spontaneous chiral symmetry breaking in metamaterials. *Nature communications* **5**, 4441 (2014).

9. Wang, Q. *et al.* Nonlinear Terahertz Generation: Chiral and Achiral Meta-Atom Coupling. *Advanced Functional Materials*, 2300639 (2023).

10. Hwang, M. *et al.* Lithography-Free Fabrication of Terahertz Chiral Metamaterials and Their Chirality Enhancement for Enantiomer Sensing. *Advanced Optical Materials*, 2300045 (2023).

11. Yang, S. *et al.* Spin-selective transmission in chiral folded metasurfaces. *Nano letters* **19**, 3432-3439 (2019).

12. Li, A., Singh, S. & Sievenpiper, D. Metasurfaces and their applications. *Nanophotonics* **7**, 989-1011 (2018).

13. Kim, Y. *et al.* Reconfigurable chiroptical nanocomposites with chirality transfer from the macro-to the nanoscale. *Nature materials* **15**, 461-468 (2016).

14. Wang, Z. *et al.* Origami-based reconfigurable metamaterials for tunable chirality. *Advanced materials* **29**, 1700412 (2017).

15. Lin, L. *et al.* All-optical reconfigurable chiral meta-molecules. *Materials Today* **25**, 10-20 (2019).

16. Chen, P. *et al.* Chirality invertible superstructure mediated active planar optics. *Nature communications* **10**, 2518 (2019).

17. Kobashi, J., Yoshida, H. & Ozaki, M. Planar optics with patterned chiral liquid crystals. *Nature Photonics* **10**, 389-392 (2016).

18. Choi, W. J., Lee, S. H., Park, B. C. & Kotov, N. A. Terahertz Circular Dichroism Spectroscopy of Molecular Assemblies and Nanostructures. *Journal of the American Chemical Society* (2022).

19. Katsantonis, I. *et al.* Strong and Broadband Pure Optical Activity in 3D Printed THz Chiral Metamaterials. *Advanced Optical Materials*, 2300238 (2023).

20. Pan, R. *et al.* Asymmetrical chirality in 3D bended metasurface. *Advanced Functional Materials* **31**, 2100689 (2021).

21. Ahmadivand, A. *et al.* Extreme sensitive metasensor for targeted biomarkers identification using colloidal nanoparticles-integrated plasmonic unit cells. *Biomed Opt Express* **9**, 373-386, doi:10.1364/BOE.9.000373 (2018).

22. Nordlander, P., Oubre, C., Prodan, E., Li, K. & Stockman, M. Plasmon hybridization in nanoparticle dimers. *Nano letters* **4**, 899-903 (2004).

23. Kravets, V., Schedin, F. & Grigorenko, A. Extremely narrow plasmon resonances based on diffraction coupling of localized plasmons in arrays of metallic nanoparticles. *Physical review letters* **101**, 087403 (2008).

24. Kravets, V. G., Kabashin, A. V., Barnes, W. L. & Grigorenko, A. N. Plasmonic surface lattice resonances: a review of properties and applications. *Chemical reviews* **118**, 5912-5951 (2018).

25. Khlopin, D. *et al.* Lattice modes and plasmonic linewidth engineering in gold and aluminum nanoparticle arrays. *JOSA B* **34**, 691-700 (2017).

26. Auguié, B. & Barnes, W. L. Collective resonances in gold nanoparticle arrays. *Physical review letters* **101**, 143902 (2008).

27. Chu, Y., Schonbrun, E., Yang, T. & Crozier, K. B. Experimental observation of narrow surface plasmon resonances in gold nanoparticle arrays. *Applied Physics Letters* **93**, 181108 (2008).

28. Stewart, J. W., Akselrod, G. M., Smith, D. R. & Mikkelsen, M. H. Toward multispectral imaging with colloidal metasurface pixels. *Advanced Materials* **29**, 1602971 (2017).

29. Mazumdar, A. & White, G. Review of cosmic phase transitions: their significance and experimental signatures. *Reports on Progress in Physics* **82**, 076901 (2019).

30. Deng, G. *et al.* From symmetry breaking to unraveling the origin of the chirality of ligated Au13Cu2 nanoclusters. *Angewandte Chemie* **130**, 3479-3483 (2018).

31. Chen, Q., Shi, J., Tao, Y. & Zernicka-Goetz, M. Tracing the origin of heterogeneity and symmetry breaking in the early mammalian embryo. *Nature communications* **9**, 1819 (2018).

32. Mason, S. The origin of chirality in nature. *Trends in Pharmacological Sciences* **7**, 20-23 (1986).

33. Jeong, K.-J. *et al.* Chirality of Fingerprints: Pattern-and Curvature-Induced Emerging Chiroptical Properties of Elastomeric Grating Meta-Skin. *ACS nano* (2022).

34. Gwak, J. *et al.* Reconfigurable Metasurface of Magnetoplasmonic Microbundle Array for Chiral Signal Enhancing. *Advanced Optical Materials*, 2202104.

35. Jeong, K.-J. *et al.* Helical Magnetic Field-Induced Real-Time Plasmonic Chirality Modulation. *ACS nano* (2020).

36. Gwak, J. *et al.* Plasmonic Enhancement of Chiroptical Property in Enantiomers Using a Helical Array of Magnetoplasmonic Nanoparticles for Ultrasensitive Chiral Recognition. *ACS Applied Materials &*

Interfaces **13**, 46886-46893 (2021).

37. Zeng, Y., Dalvit, D., O'hara, J. & Trugman, S. Modal analysis method to describe weak nonlinear effects in metamaterials. *Physical Review B* **85**, 125107 (2012).

38. Raman, A. & Fan, S. Photonic band structure of dispersive metamaterials formulated as a Hermitian eigenvalue problem. *Physical review letters* **104**, 087401 (2010).

39. Chowdhury, D. R. *et al.* Excitation of dark plasmonic modes in symmetry broken terahertz metamaterials. *Optics express* **22**, 19401-19410 (2014).

40. Azad, A. K., Taylor, A. J., Smirnova, E. & O'Hara, J. F. Characterization and analysis of terahertz metamaterials based on rectangular split-ring resonators. *Applied Physics Letters* **92**, 011119 (2008).

41. Nguyen, H.-Q. *et al.* One-Pot Synthesis of Magnetoplasmonic Au@ Fe x O y Nanowires: Bioinspired Bouligand Chiral Stack. *ACS nano* (2022).

42. Liu, N. *et al.* Planar metamaterial analogue of electromagnetically induced transparency for plasmonic sensing. *Nano letters* **10**, 1103-1107 (2010).

43. Meinzer, N., Barnes, W. L. & Hooper, I. R. Plasmonic meta-atoms and metasurfaces. *Nature photonics* **8**, 889-898 (2014).

44. Jones, K. A. *et al.* Orthogonal luciferase−luciferin pairs for bioluminescence imaging. *Journal of the American Chemical Society* **139**, 2351-2358 (2017).

45. Liu, C. *et al.* High-performance bifunctional polarization switch chiral metamaterials by inverse design method. *npj Computational Materials* **5**, 93 (2019).

46. Nguyen, H.-Q. *et al.* One-Pot Synthesis of Magnetoplasmonic Au@ Fe x O y Nanowires: Bioinspired Bouligand Chiral Stack. *ACS nano* **16**, 5795-5806 (2022).

47. Shin, H. J., Oh, S. J., Lim, M.-C., Choi, S.-W. & Ok, G. Dielectric traces of food materials in the terahertz region. *Infrared Physics & Technology* **92**, 128-133 (2018).

Scheme

Scheme 1 is available in the Supplementary Files section.

Figures
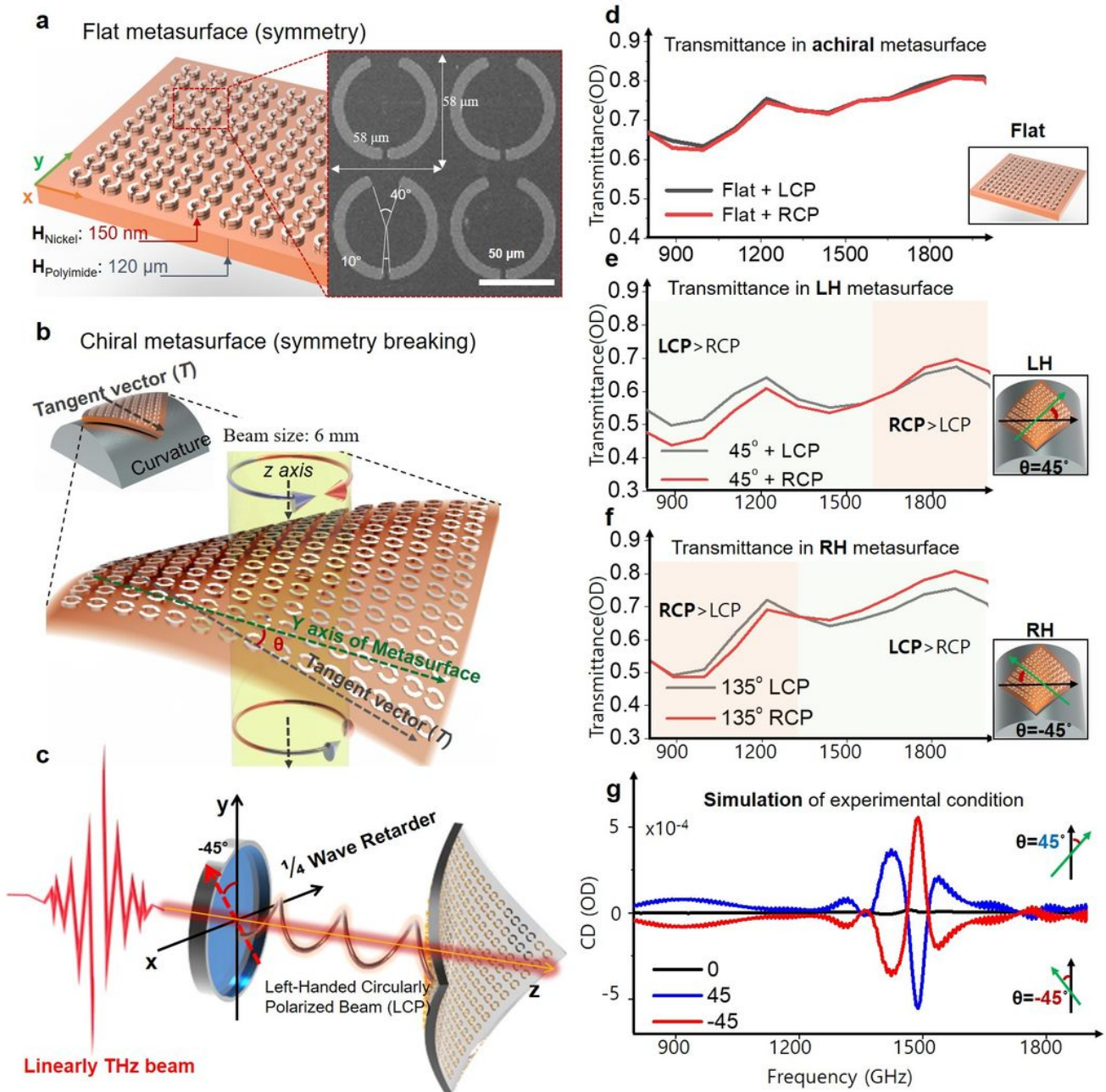
Figure 1

Schematic illustrations of the metasurfaces for reconfigurable THz chiroptical properties.

(a) The Schematic illustration and SEM image of Ni split-ring metasurfaces (SRMs). (b) Schematic of chiral THz metasurface with curvature. The θ is skew angle between Y axis of metasurface (Y) and tangent vector of curvature (T). (c) THz circularly polarized beam for metasurface response. THz-time domain spectroscopy spectra; The left and right circular polarized THz-time domain spectroscopy spectra of (d) achiral, (e) Left handed (LH) and (f) right handed (RH) chiral Ni split-ring metasurface. (g) Computational CD spectra of chiral metasurface with experimental condition.
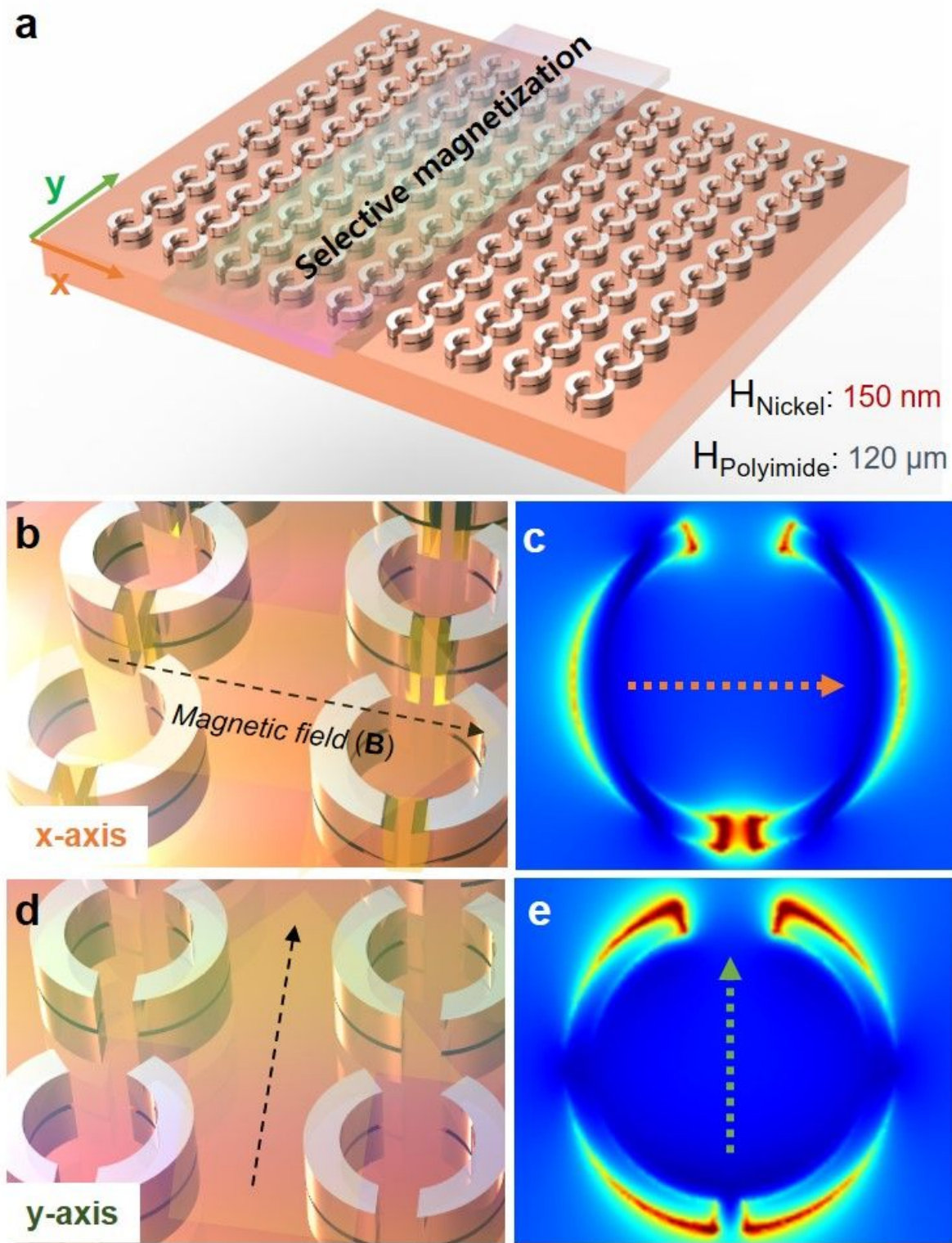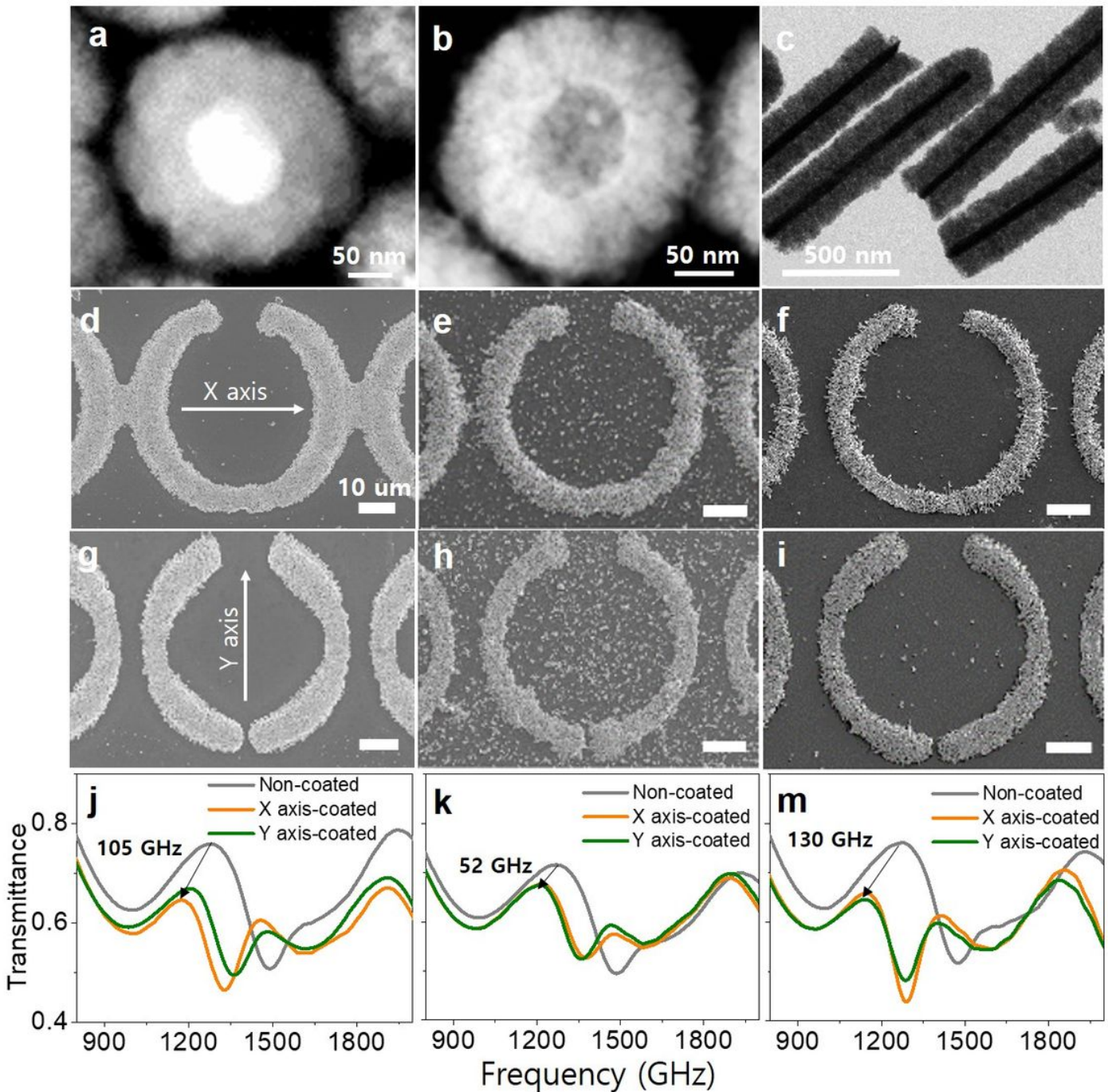
Figure 2

The regioselective magnetization of Ni SRMs.

(a) Schematic geometric dimensions of Ni SRM. The experimental scheme and the magnetization simulation of the metasurface depending on the (b, c) *X*- and (d, e) *Y*-axis direction of magnetic field.
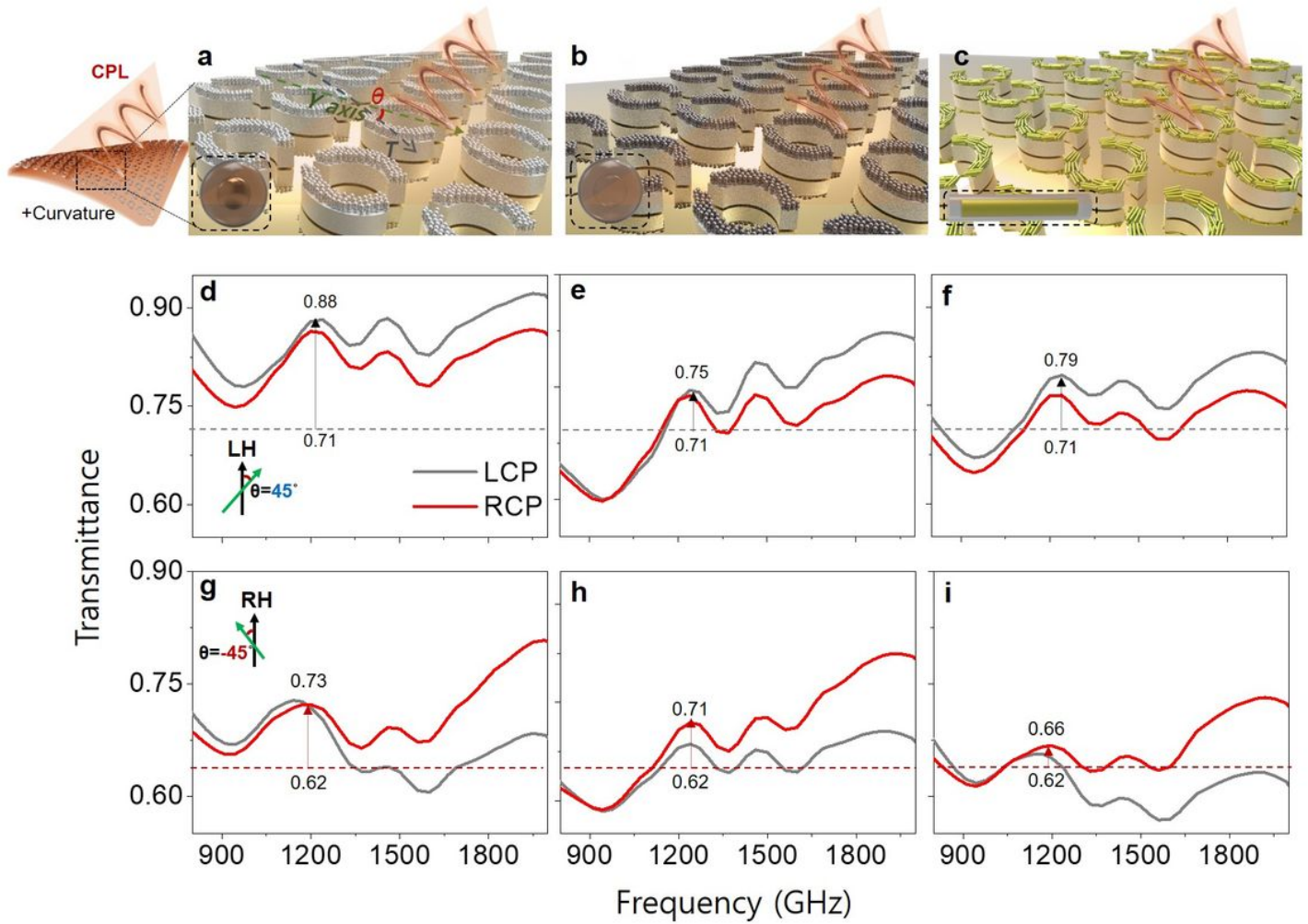
Figure 3

Regioselective assembly of MagPlas NP/NR on Ni-metasurface depending on the magnetization direction at X and Y.

(a) TEM images of Ag@Fe$_3$O$_4$ MagPlas NPs, (b) its hollow (void@Fe$_3$O$_4$) NPs, where the Ag core was etched out, and (c) Au@Fe$_3$O$_4$ MagPlas nanorods. SEM image of regioselective metasurface of (d, g) Ag@Fe$_3$O$_4$ NPs, (e, h) hollow NPs, and (f, i) Au@Fe$_3$O$_4$ NRs. THz-time domain spectroscopy spectra of (j) MagPlas (Ag@Fe$_3$O$_4$) and (k) hollow NPs, and (m) Au@Fe$_3$O$_4$ NRs in the Ni-metasurface depending on the magnetization direction (X and Y).
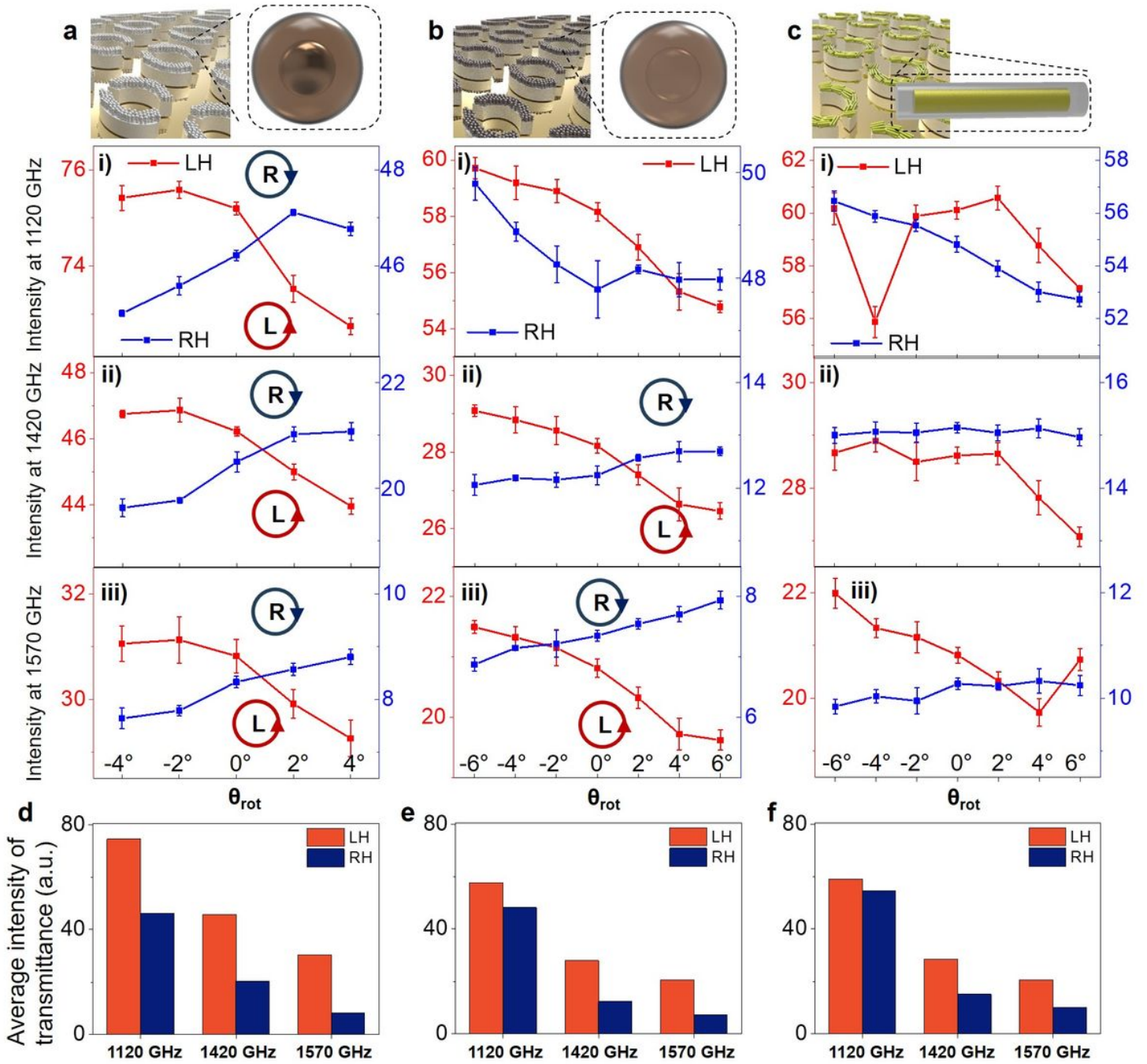
Figure 4

The selective chiral plasmonic metasurface for THz signal enhancement.

The reconfigurable chiral metasurface composed of (a) Ag@Fe$_3$O$_4$ NPs, (b) hollow NPs, and (c) Au@Fe$_3$O$_4$ NRs. FFT applied to the magnitude-frequency data of (d, g) Ag@Fe$_3$O$_4$ NPs, (e, h) hollow NPs and (f, i) Rod on LH and RH metasurface using circular polarized THz-time domain spectroscopy spectra.

Figure 5

Optical activity characterization of the polarization state of the transmitted THz linear waves through regioselective chiral metasurface.

FFT analysis for the (a) Ag@Fe$_3$O$_4$ NPs, (b) Hollow NPs, and (c) Au@Fe$_3$O$_4$; The graph represents the FFT analysis conducted on the magnitude of transmittance variation as a function of frequency. The analysis is performed at a frequency of 1120, 1420, and 1570 GHz while varying the rotation angle (θ_{rot}). THz Transmittance Correlation with LH and RH Structures: (d) MagPlas NPs, (e) Hollow NPs, and (f) MagPlas NRs.

Supplementary Files

This is a list of supplementary files associated with this preprint. Click to download.

- ChiralTHzreconfigurablemetasurfaceS.lfinal.docx
- Scheme1.jpeg